A separate fit for $R_h < 2$ AU ($Q_{CO} = (2.07 \times 10^{30})R_h^{-1.66\pm0.22}$) shows the same heliocentric dependence, and is displaced above the 'native' fit by a factor of ~2. Thus the present analysis suggests approximately equal contributions from native and distributed sources to the total CO production in comet Hale–Bopp within $R_h \sim 1.5$ AU (Table 1).

Could the onset of a distributed source for CO be related to a change in dust production or destruction? Our measurements of dust (at 4.7 μm wavelength) sample particles with sizes of a few micrometres, and follow a heliocentric dependence ($Q_{dust} \propto R_h^{-2.73\pm0.12}$) which is steeper than our findings for Q_{CO} and Q_{H_2O} (see note added in proof, below). This implies a rapid increase in dust fragmentation, and hence a decrease in mean particle size, with decreasing heliocentric distance. (In our analysis, we have assumed the same heliocentric dependence of outflow velocity ($R_h^{-0.5}$) for dust and gas.) Detailed modelling of dust properties (outflow, composition, destruction) convolved with geometrical effects, will be reported elsewhere.

If the onset of distributed CO emission was related to increased dust release as the comet approached perihelion, a sharp increase (that is, a 'jump') in Q_{dust} similar to that observed for Q_{CO} between 2.02 and 1.48 AU would be expected. Whereas Q_{CO} follows two distinct distributions—one for $R_h < 2$ AU and another for $R_h > 2$ AU—Q_{dust} appears to fit a single distribution, with no such jump near (or inside) $R_h = 2$ AU.

The lack of a jump in Q_{dust} near $R_h = 2.0$–1.5 AU demonstrates that the onset of distributed CO emission cannot be explained by increased dust production alone. Rather, it is plausible that a threshold (most likely thermal) is reached for release of additional CO in the coma. The similar power-law dependence exhibited by Q_{CO} for both $R_h < 2$ AU and $R_h > 2$ AU, and by Q_{H_2O} (ref. 17), suggests that release of the 'parent' giving rise to distributed CO is controlled by sublimation of the same nuclear ice as seen for other native volatiles (water, native CO). We thus infer that the distributed parent has a constant mixing ratio in the nucleus relative to native H_2O and CO ices.

The difference between the Q-curves for CO and (scaled) dust approximates the Q-curve for the distributed component alone. This reaches its terminal value at a projected distance $\rho \approx 6.5 \times 10^3$ km from the nucleus for $R_h = 1.48$ AU, and at $\sim 5.1 \times 10^3$ km for $R_h = 1.06$ AU. The distance ρ approximates the scale for release of distributed CO, and can be compared with model predictions to better constrain the scale length of the distributed parent. Future refinements[21–24] to our analytical approach include accounting for axisymmetric outflow and for gas acceleration in the coma. We expect such modelling to have relatively little effect on our retrieved amount of native CO, but it should provide significant improvements to our understanding of the distributed source.

We have characterized the release of carbon monoxide in comet Hale–Bopp, and compared it with water and dust. Within $R_h \approx 1.5$ AU, our results support a dual-source nature for CO production, as seen first in comet Halley during the Giotto spacecraft encounter[6]. We infer a total (native plus distributed) mean CO production rate of 24.1 ± 0.9% relative to water, with 51 ± 3% of the observed CO contained in the nuclear ice, the remainder being produced in the coma.

Note added in proof: Production of millimetre-sized dust in comet Hale–Bopp follows a single distribution with power law $R_h^{-1.7\pm0.2}$ for R_h between 0.9 and 2.5 AU (ref. 32). This heliocentric slope is consistent with those we derive for Q_{CO} and Q_{H_2O}, and this supports uniform mixing of volatile and refractory components in the nucleus. □

Received 17 November 1998; accepted 12 April 1999.

1. Rank, D. M., Townes, C. H. & Welch, W. J. Interstellar molecules and dense clouds. *Science* **174,** 1083–1101 (1971).
2. Turner, B. E. Recent progress in astrochemistry. *Space Sci. Rev.* **51,** 235–337 (1989).
3. Mumma, M. J. Organic volatiles in comets: Their relation to interstellar ices and solar nebula material. *Astron. Soc. Pacif. Conf. Ser.* **122,** 369–396 (1997).
4. Mumma, M. J., Weissman, P. R. & Stern, S. A. in *Protostars and Planets, III* (eds Levy, E. H. & Lunine, J. I.) 1177–1252 (Univ. Arizona Press, Tucson, 1993).
5. Sandford, S. A. & Allamandola, L. J. The condensation and vaporization behavior of H_2O:CO ices and implications for interstellar grains and cometary activity. *Icarus* **76,** 201–224 (1988).
6. Eberhardt, P. *et al.* The CO and N_2 abundance in comet P/Halley. *Astron. Astrophys.* **187,** 481–484 (1987).
7. Huebner, W. F., Boice, D. C. & Sharp, C. M. Polyoxymethylene in comet Halley. *Astrophys. J.* **320,** L149–L152 (1987).
8. Huntress, W. T., Allen, M. & Delitsky, M. Carbon suboxide in comet Halley? *Nature* **352,** 316–318 (1991).
9. Meier, R., Eberhardt, P., Krankowsky, D. & Hodges, R. R. The extended formaldehyde source in comet P/Halley. *Astron. Astrophys.* **277,** 677–690 (1993).
10. Greenberg, J. M. & Li, A. From interstellar dust to comets: the extended CO source in comet Halley. *Astron. Astrophys.* **332,** 374–384 (1998).
11. Chiar, J. E. *et al.* Processing of icy mantles in protostellar envelopes. *Astrophys. J.* **498,** 716–727 (1998).
12. Biver, N. *et al.* Substantial outgassing of CO from comet Hale–Bopp at large heliocentric distance. *Nature* **380,** 137–139 (1996).
13. Biver, N. *et al.* Evolution of the outgassing of comet Hale–Bopp (C/1995 O1) from radio observations. *Science* **275,** 1915–1918 (1997).
14. Womack, M., Festou, M. C. & Stern, S. A. The heliocentric evolution of key species in the distantly-active comet C/1995 O1 (Hale–Bopp). *Astron. J.* **114,** 2789–2795 (1997).
15. Greene, T. P., Tokunaga, A. T., Toomey, D. W. & Carr, J. S. CSHELL: A high spectral resolution 1–5 μm cryogenic echelle spectrograph for the IRTF. *Proc. SPIE* **1946,** 311–324 (1993).
16. Dello Russo, N., DiSanti, M. A., Mumma, M. J., Magee-Sauer, K. & Rettig, T. W. Carbonyl sulfide in comets C/1996 B2 (Hyakutake) and C/1995 O1 (Hale–Bopp): Evidence for an extended source in Hale–Bopp. *Icarus* **135,** 377–388 (1998).
17. Dello Russo, N. *et al.* Direct detection of water in comet C/1995 O1 (Hale–Bopp). *Icarus* (submitted).
18. Herzberg, G. *Spectra of Diatomic Molecules* (Van Nostrand Reinhold, New York, 1950).
19. Weaver, H. A. *et al.* Infrared spectroscopy of comet Hale–Bopp. *Earth Moon Planets* (in the press).
20. Lämmerzahl, P. *et al.* Expansion velocity and temperatures of gas and ions measured in the coma of comet P/Halley. *Astron. Astrophys.* **187,** 169–173 (1987).
21. Boice, D. C., Sablik, M. J. & Konno, I. Distributed coma sources and the CH_4/CO ratio in Comet Halley. *Geophys. Res. Lett.* **17,** 1813–1816 (1990).
22. Crifo, J. F. A general physicochemical model of the inner coma of active comets. 1. Implications of spatially distributed gas and dust production. *Astrophys. J.* **445,** 470–488 (1995).
23. Xie, X. & Mumma, M. J. Monte Carlo simulation of cometary Atmospheres: Application to Comet P/Halley at the time of the Giotto Spacecraft encounter. II. Axisymmetric model. *Astrophys. J.* **464,** 457–475 (1996).
24. Combi, M. R. Time-dependent gas kinetics in tenuous planetary atmospheres: The cometary coma. *Icarus* **123,** 207–226 (1996).
25. Xie, X. & Mumma, M. J. The effect of electron collisions on rotational populations of cometary water. *Astrophys. J.* **386,** 720–728 (1992).
26. Biver, N. *et al.* Long term evolution of the outgassing of comet Hale–Bopp from radio observations. *Earth Moon Planets* (in the press).
27. Kunde, V. G. & Maguire, W. C. A direct integration transmittance model. *J. Quant. Spectrosc. Rad. Transf.* **14,** 803–817 (1974).
28. Rothman, L. S. *et al.* The HITRAN molecular database: Editions of 1991 and 1992. *J. Quant. Spectrosc. Rad. Transf.* **48,** 469–507 (1992).
29. Crovisier, J. Rotational and vibrational synthetic spectra of linear parent molecules in comets. *Astron. Astrophys. Suppl.* **68,** 223–258 (1987).
30. Huebner, W. F., Keady, J. J. & Lyon, S. P. Solar photo rates for planetary atmospheres and atmospheric pollutants. *Astrophys. Space Sci.* **195,** 1–294 (1992).
31. Green, S. F., McDonnell, J. A. M., Pankiewicz, G. S. A. & Zarnecki, J. C. in *20th ESLAB Symposium on the Exploration of Halley's Comet* Vol. 2, 81–86 (SP-250, ESA, 1986).
32. Jewitt, D. & Matthews, H. E. Particulate mass loss from comet Hale–Bopp. *Astron. J.* **117,** 1056–1062 (1999).

Acknowledgements. This work was supported through the NASA Planetary Astronomy Program. We thank the staff of the NASA Infrared Telescope Facility for their support throughout our comet Hale–Bopp observing campaign. The IRTF is operated by the University of Hawaii under contract to NASA. We thank J. Crovisier for comments which improved the manuscript.

Correspondence and requests for materials should be addressed to M.D. (e-mail: disanti@kuiper.gsfc.nasa.gov).

Collective and plastic vortex motion in superconductors at high flux densities

A. M. Troyanovski*†, J. Aarts* & P. H. Kes*

** Kamerlingh Onnes Laboratory, Leiden University, PO Box 9504, 2300 RA Leiden, The Netherlands*
† Institute for High Pressure Physics, Russian Academy of Science, Troitsk, 142092, Russia

The 'mixed state' of type II superconductors occurs when magnetic flux penetrates the material (in the form of vortices) without destroying the superconducting ground state. Zero resistivity is retained if the vortices are pinned by crystalline defects, but is destroyed by vortex motion. This provides the practical motivation for studying vortices in random pinning potentials[1–7]. But the insights so obtained also bear on the more general class of problems involving the dynamics of elastic media in the presence

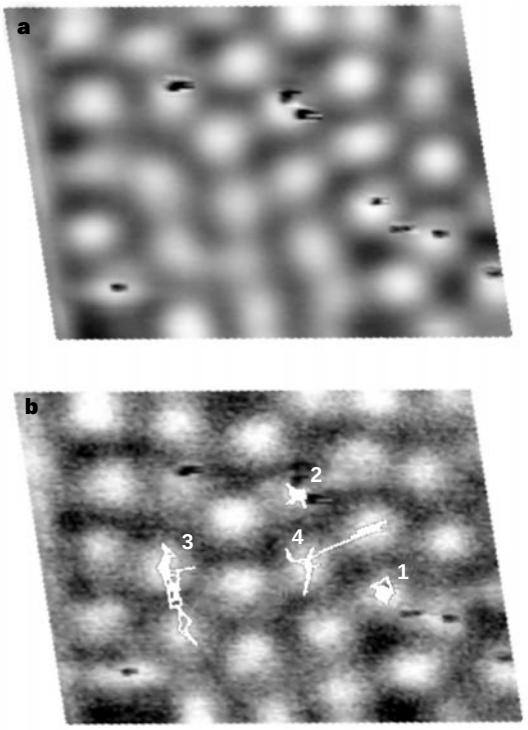

Figure 1 STM image (420 × 280 nm) at $B = 0.6$ T of plastic flow of the vortex lattice in $NbSe_2$ containing columnar defects (CDs). The CDs are seen as black dots, their concentration is $B_\phi = 0.3$ T (at B_ϕ the areal density of vortices equals that of the CDs). Panel **a** shows an average over 128 subsequent images, resulting in a grey scale representing the probability density for finding a vortex at a certain position. Several trajectories of plastic flow can be recognized. Panel **b** shows the trajectories of four typical vortices as obtained from images 0–35. See text for details of these vortices.

of quenched disorder[8] (for example, mechanical friction). Moreover, the magnetic vortex system is highly tunable and permits questions concerning frictional, plastic and elastic flow[9] to be investigated on the scale of single vortices. Remarkable results have been obtained on the dynamics of this system[10–17], but have been largely restricted to well separated vortices at very low flux densities. Scanning tunnelling microscopy has the potential to resolve individual vortices at much higher flux densities[18–21], and here we show that the imaging rates can be sufficiently high to resolve the dynamics in this flux regime. We find that, in the presence of strongly pinning line defects, the vortex lattice remains pinned until the number of vortices is about twice that of the defects, at which point plastic creep commences. But in the presence of weak intrinsic point disorder, the vortices creep coherently along one of the principle axes of the vortex lattice, where they exhibit striking and unanticipated velocity modulations that appear to be related to the lattice periodicity.

Our scanning tunnelling microscope (STM) experiments were all performed at 4.3 K in fields B up to 1.9 T. From SQUID (superconducting quantum interference device) magnetization measurements on a pristine $NbSe_2$ crystal, we determined a critical temperature $T_c = 7.10$ K and an upper critical field $\mu_0 H_{c2}(4.3\,\mathrm{K}) = 2.13$ T. The coherence length ξ at 4.3 K is therefore 12.5 nm and the vortex core diameter about 35 nm (ref. 22). Several crystals were irradiated with 6-GeV Pb ions in order to create columnar defects (CDs). Two doses were used, corresponding to B_ϕ of 0.2 and 0.3 T (at B_ϕ the areal density of vortices equals that of the CDs). The typical sample size was about 2 × 2 mm and the thickness ranged between 0.1 and 0.5 mm. The thinnest crystals were used for the ion irradiation to ensure that the CDs traverse the entire sample. Before the experiment, the sample was mounted onto the sample holder and cleaved under ambient conditions. Our STM is designed as an insert to a helium transport vessel, similar to that described in ref. 23. The STM with sample was cooled down to 4.3 K in zero applied field by slowly immersing it into liquid helium. A superconducting coil was used to generate a magnetic field in the direction of the CDs and perpendicular to the sample surface.

The STM tip was positioned somewhere between the edge and the centre of the sample. Vortices were imaged using a cut Pt–Ir tip both in topographic mode (constant current) and current mode (constant average current). They appear, depending on B, as hills of height 0.1–2 Å because of the modulation of the tunnelling conductance associated with the order-parameter variations of the vortex lattice. With increasing B, the amplitude of the modulation decreases and the images become more noisy. Tunnelling currents between 15 and 25 pA and a tip–sample bias voltage of 0.5–1 mV were used. For a scanning area of 400 × 400 nm with 128 lines the scanning time was $\geqslant$3 s. Data storage took 3.3 s so that the total acquisition time of one image could be as small as 6.5 s. Usually it was ~10 s. This fast scanning operation allowed us to observe moving vortices by STM compiled in a cartoon-like fashion as vortex movies; see Supplementary Information.

The raw data seem to show a somewhat distorted vortex lattice; but a hexagonal vortex arrangement results after a correction is made for the spatial distortions of our microscope in the x–y plane. The scaling factors were determined by comparing the image of the $NbSe_2$ lattice with the crystallographic atom arrangement. The field calibration was carried out at fields close to H_{c2} where the demagnetization correction is negligible. The position of the CDs in irradiated samples provided information about the mechanical stability of the STM and sample holder. As there was no visible displacement of CDs in the images, we estimate the instability to be less than 1–2 pixels.

The STM images contain both topographic and spectroscopic information, and it is possible to see CDs and vortices simultaneously. The defects are visible as black spots (see Fig. 1) with diameters that appear to be 10–20 nm, but this is an artefact of our experiment; it is known[30] that the track diameter is about 7.0–9.0 nm. The distribution of defects is random with large fluctuations, which explains why in Fig. 1 we only observe half the average number (~16) expected for this area. Because of the competition between pinning energy and deformation energy, the occupation number at $B \approx B_\phi$ is only 50% (ref. 24). For the same reason the vortex arrangement at $B < B_\phi$ is very disordered[25]. At fields far above B_ϕ the vortex configurations approaches that of a granular triangular lattice with (strong) perturbations at the sites of the CDs.

To study vortex motion in the sample with $B_\phi = 0.3$ T, we collected data consecutively at fields of 0.6, 0.5, 0.4, 0.3 and 0.2 T after coming down from 1.0 T and waiting 20 min each time before making measurements. The same area, shown in Fig. 1, was repeatedly probed. The vortex lattice at all fields was highly disordered. For fields up to 0.5 T, essentially all vortices remain pinned during the observation time (500 s). Even a disordered vortex lattice does not lose its integrity when only ~1/3 of its vortices are trapped on a CD, revealing that the effective shear modulus is still appreciable. At 0.6 T plastic flow sets in, as is seen in Fig. 1a which shows an average over 128 subsequent images. The grey scale thus represents the probability of finding a vortex at a certain position. In the lower left corner is one of the flow paths of vortices moving through more strongly pinned neighbours. In Fig. 1b we show the vortex motion by marking the subsequent positions (for frames 0–35) of four typical vortices: vortex 1, pinned by 1 CD; vortex 2, pinned by 2 CDs; vortex 3 in a path of plastic flow; and vortex 4, which occasionally slips through between vortices 1 and 2. We note that 'vortex 3' in fact represents three different vortices which subsequently move along the same path. When we concentrate on vortex 1, we see that it moves isotropically in the

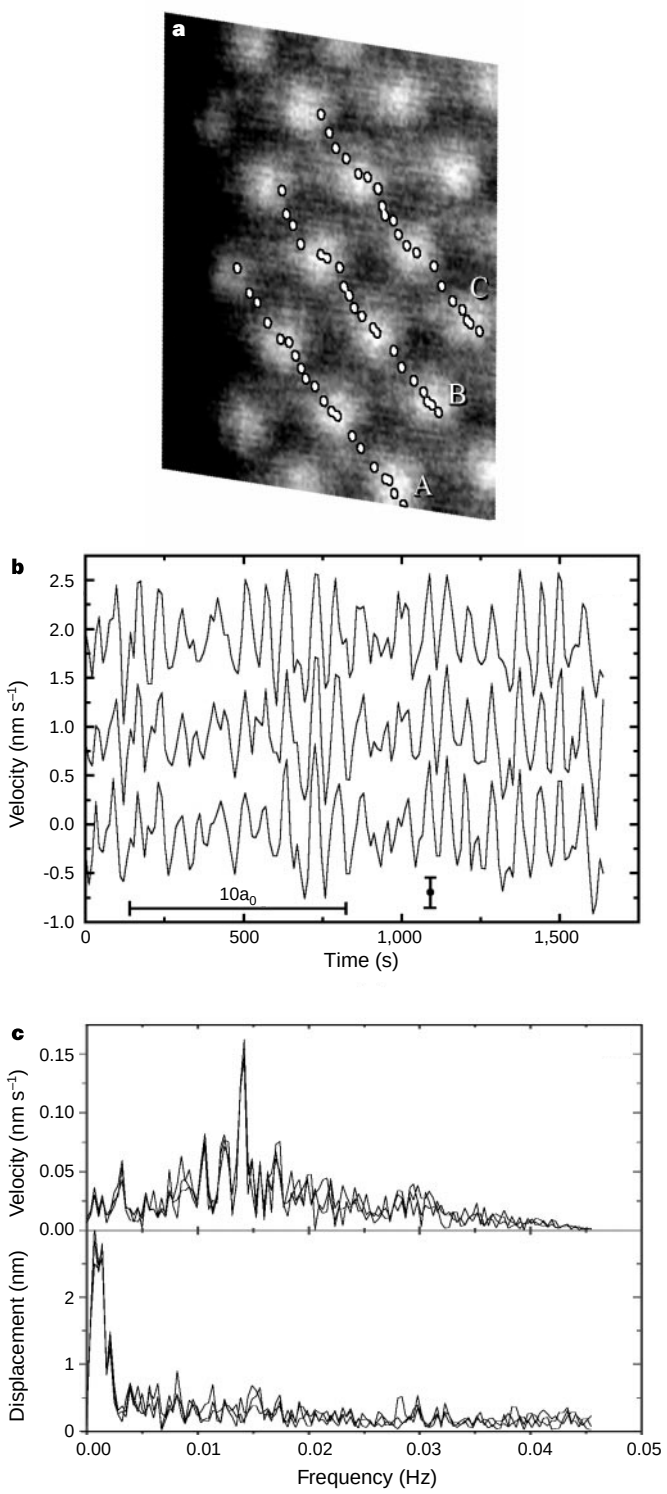

Figure 2 STM image (230 × 355 nm) of a moving vortex lattice in pristine $NbSe_2$ at a field 0.6 T. **a**, Frame no. 85 out of a sequence of 168 images. The dots represent the subsequent positions of three vortices (A, B, C) as determined from frames nos 84–103. Imaging time for each frame is 6.5 s, repetition time is 11 s. **b**, The longitudinal velocity of the three vortices in **a** versus time (data for vortices A and C are shifted over $\pm$ 1.0 nm s^{-1} for clarity). A velocity modulation with period a_0 (the vortex lattice parameter) can be clearly identified. **c**, Fourier transforms of the longitudinal velocity (after subtracting the average value of v to suppress the peak at zero frequency) and the transverse displacements of the same vortices A, B and C. The peak at 14.1 mHz in the upper panel reveals the "washboard" frequency (see text) at v/a_0 for the longitudinal velocity and displacements. No peak is seen for the transverse displacements in the lower panel. Here the low-frequency peaks are displaying the long-timescale (700–1,500 s) fluctuations.

potential well caused by the CD as it is pushed around by its moving neighbours. The motion of vortex 2 is more anisotropic, with a larger amplitude parallel to the line connecting the two CDs on which it is pinned. The average distance between vortex 1 and 2 is 115 nm; this is slightly smaller than $2a_0$ (= 126 nm), where $a_0 = (2\Phi_0/\sqrt{3}B)^{1/2}$ is the vortex lattice parameter and Φ_0 the flux quantum. This prohibits the movement of vortex 4. However, the displacement fluctuations caused by the other moving vortices may add roughly 13 nm to the average distance, allowing vortex 4 to slip through and follow a path that seems to merge with that of vortex 3.

For the pristine $NbSe_2$ crystals, almost perfect hexagonal vortex lattices were observed in a wide range of magnetic fields. Figure 2a shows a typical image: it was taken 20 min after the field was increased from 0 to 0.6 T and the persistent mode switch turned on. It contains 22 vortices, and is one of 168 subsequent images each taking 11 s yielding a total recording time of 30 min. It is remarkable that the 22 vortices move coherently as one bundle. Twenty subsequent positions of three vortices (A, B, C) are denoted by the white dots. Within experimental error they each represent the motion of the entire bundle. We convinced ourselves by decreasing the scan rate that we are not observing some stroboscopic effect but that we are really detecting the average velocity v. Its mean value is about $a_0/6$ per frame, yielding $v \approx 1.0\,\mathrm{nm\,s^{-1}}$ and an electric field $E = vB \approx 0.6\,\mathrm{nV\,m^{-1}}$. This value is 5 orders of magnitude smaller than the commonly used voltage criterion defining the critical current density j_c. The motion can be self-consistently[26] described as collective creep with a resistivity $\rho \approx \rho_f \exp[-U(j)/k_B T]$ where ρ_f is the flux flow resistivity. The actual energy barrier $U(j)$ and current density j turn out to be $j \approx 0.4 j_c \approx 2.3 \times 10^6\,\mathrm{A\,m^{-2}}$ and $U \approx 77$ K. The transverse size R_A of the region in which positional short-range order persists in absence of topological defects can be estimated, assuming collective pinning[27], to be $R_A \approx R_c(a_0/\xi\sqrt{2})^{4-d}$, where R_c is the transverse Larkin length[27] and d the dimensionality of the vortex lattice disorder. With $R_c \approx 3a_0$ (ref. 28) we obtain $R_A \approx 36a_0$ for $d = 3$, or $R_A \approx 10a_0$ for $d = 2$. Our observation of a perfect vortex lattice consisting of 22 vortices falls well within this estimate, irrespective of d. Finally, it is seen that the mean distance the vortex bundle has moved between frames is ~12 nm, which is quite close to the value of ξ at 4.3 K. This observation fits with the picture of creep in which vortex bundles hop between local minima in the random pinning potential which has the coherence length as the shortest relevant length scale.

The vortex lattice is seen (Fig. 2a) to move along one of its principle axes. This seems to be in agreement with the minimum dissipation argument of Schmid and Hauger[29] for a vortex lattice moving with large velocity (flow regime) through a random potential. However, it is unlikely that this argument should hold for the creep regime as well. On the other hand, in equilibrium, the orientations of the vortex lattice and the underlying crystal lattice of $NbSe_2$ coincide[18] because both have hexagonal symmetry. This coincidence, which we indeed observe, will impose an additional 'tin roof' potential on the moving vortex lattice thus fixing its orientation, but still allowing sliding motion when the driving force f_d is not aligned with the principle axis. We do not know the direction of f_d, but it is quite unlikely that it would have been directed along a principle axis of the vortex lattice in all our experiments. Nevertheless, we do not see sliding motion. Our data therefore rather support the predictions of Le Doussal and Giamarchi[3,4] that a slowly moving glass at finite temperatures behaves like a moving glass at $T = 0$, that is, it moves along rough channels (see below) which are stable against a small transverse force component.

Our most important result follows from plotting the positions of the vortices A, B and C versus time. When they moved out of the field of view we added na_0, with integer n, to the position of the corresponding vortex that just appeared in the picture. This procedure is allowed because the vortices move coherently with

well known average velocity ($v = 0.89\,\mathrm{nm\,s^{-1}}$) and orientation. Taking the derivative of these trajectories yields a plot of the longitudinal velocities versus time (Fig. 2b). For clarity, we shifted the results for vortex A and C by $\pm 1\,\mathrm{nm\,s^{-1}}$. The error bar denotes the uncertainty in v ($\delta v = \pm 0.15\,\mathrm{nm\,s^{-1}}$) due to the error in the vortex positions. The horizontal bar marks the time needed to traverse a distance $10a_0$ (630 nm). It is clearly seen that the velocity is modulated with a periodic component with amplitude $\Delta v \approx 0.6\,\mathrm{nm\,s^{-1}}$ and period a_0/v. In the Fourier transform (Fig. 2c), this shows up as a peak at 14.1 mHz. Such a peak at the "washboard" frequency is known for periodic structures driven through random point disorder[9], but to the best of our knowledge this is the first time that this washboard feature has been found to survive in the creep regime. The periodic modulation also appears in the longitudinal displacement determined with respect to the average, uniform motion versus time. However, it is not observed in a plot of the transverse displacements versus time. Rather, we see on our timescale a random-walk-like transverse excursion of the bundle up to an amplitude $0.2a_0$, not yet enough to decide how the mean-squared displacement grows with time. We leave this for future investigations.

Fast imaging of vortex lattices by STM provides the possibility of studying the collective and plastic flow behaviour of elastic media through various configurations of disorder. □

Received 7 December 1998; accepted 5 April 1999.

1. Blatter, G. *et al.* Vortices in high-temperature superconductors. *Rev. Mod. Phys.* **66,** 1125–1388 (1994).
2. Koshelev, A. E. & Vinokur, V. M. Dynamic melting of the vortex lattice. *Phys. Rev. Lett.* **73,** 3580–3583 (1994).
3. Giamarchi, T. & LeDoussal, P. Moving glass phase of driven lattices. *Phys. Rev. Lett.* **76,** 3408–3411 (1996).
4. Le Doussal, P. & Giamarchi, T. Moving glass theory of driven lattices with disorder. *Phys. Rev. B* **57,** 11356–11403 (1998).
5. Moon, K., Scalettar, R. & Zimámny, G. T. Dynamical phases of driven vortex systems. *Phys. Rev. Lett.* **77,** 2778–2781 (1996).
6. Scheidl, S. & Vinokur, V. M. Driven dynamics of periodic elastic media in disorder. *Phys. Rev. B* **57,** 13800–13810 (1998).
7. Balents, L., Marchetti, M. C. & Radzikovsky, L. Nonequilibrium steady states of driven periodic media. *Phys. Rev. B* **57,** 7705–7739 (1998).
8. Nattermann, T. Scaling approach to pinning; Charge-density waves and giant flux creep in superconductors. *Phys. Rev. Lett.* **64,** 2454–2457 (1990).
9. Olsen, C. J., Reichhardt, C. & Nori, F. Nonequilibrium dynamics phase diagram for vortex lattices. *Phys. Rev. Lett.* **81,** 3757–3760 (1998).
10. Osakabe, N., Kasai, H., Kodama, T. & Tonomura, A. Time-resolved analysis in transmission electron microscopy and its application to the study of the dynamics of vortices. *Phys. Rev. Lett.* **78,** 1711–1714 (1997).
11. Kirtley, J. R. *et al.* Direct imaging of integer and half-integer Josephson vortices in high-T_c grain boundaries. *Phys. Rev. Lett.* **76,** 1336–1339 (1996).
12. Oral, A. *et al.* Direct observation of melting of the vortex solid in $Bi_2Sr_2CaCu_2O_{8+\delta}$ single crystals. *Phys. Rev. Lett.* **80,** 3610–3613 (1998).
13. Mozer, A. *et al.* Observation of single vortices condensed into a vortex-glass phase by magnetic force microscopy. *Phys. Rev. Lett.* **74,** 1847–1850 (1995).
14. Bolle, C. A., de la Cruz, F., Gammel, P. L., Waszczak, J. V. & Bishop, D. J. Observation of tilt induced orientational order in the magnetic flux lattice 2*H*-$NbSe_2$. *Phys. Rev. Lett.* **71,** 4039–4042 (1993).
15. Yao, Z. *et al.* Path of magnetic flux lines through high-T_c copper oxide superconductors. *Nature* **371,** 777–779 (1994).
16. Marchevsky, M. V., Aarts, J., Kes, P. H. & Indenbom, M. V. Observation of the correlated vortex flow in $NbSe_2$. *Phys. Rev. Lett.* **78,** 531–534 (1997).
17. Pardo, F. *et al.* Real space images of the vortex lattice structure in a Type II superconductor during creep over a barrier. *Phys. Rev. Lett.* **79,** 1369–1372 (1997).
18. Hess, H. F., Robinson, R. B. & Waszczak, J. V. Vortex-core structure observed with a scanning tunneling microscope. *Phys. Rev. Lett.* **64,** 2711–2714 (1990).
19. Maggio-Aprile, I., Renner, Ch., Erb, A., Walker, E. & Fischer, Ø. Direct vortex lattice imaging and tunneling spectroscopy of flux lines on $YBa_2Cu_3O_{7-\delta}$. *Phys. Rev. Lett.* **75,** 2754–2757 (1995).
20. Renner, Ch., Revaz, B., Kadowaki, K., Maggio-Aprile, I. & Fischer, Ø. Observation of the low temperature pseudogap in the vortex cores of $Bi_2Sr_2CaCu_2O_{8+\delta}$. *Phys. Rev. Lett.* **80,** 3606–3609 (1998).
21. De Wilde, Y. *et al.* Scanning tunneling microscopy observation of a square Abrikosov lattice in $LuNi_2B_2C$. *Phys. Rev. Lett.* **78,** 4273–4276 (1997).
22. Volodin, A. P., Golubov, A. A. & Aarts, J. Vortex core shapes measured by STM. *Z. Phys. B* **102,** 317–321 (1997).
23. Volodin, A. P. & Troyanovski, A. M. A three-phase piezoinertio motor for a low temperature STM. *Instr. Exp. Techn.* **40,** 724–726 (1997).
24. Wengel, C. & Tauber, U. C. Weakly pinned Bose glass vs Mott insulator phase in superconductors. *Phys. Rev. Lett.* **78,** 4845–4848 (1997).
25. Behler, S. *et al.* Vortex pinning in ion-irradiated $NbSe_2$ studied by scanning tunneling microscopy. *Phys. Rv. Lett.* **72,** 1750–1753 (1994).
26. van der Beek, C. J., Nieuwenhuys, G. J. & Kes, P. H. Nonlinear current diffusion in type-II superconductors. *Physica C* **197,** 320–336 (1992).
27. Larkin, A. I. & Ovchinnikov, Yu. N. Pinning in type II superconductors. *J. Low Temp. Phys.* **34,** 409–427 (1979).
28. Angurel, L. A., Amin, F., Polichetti, M., Aarts, J. & Kes, P. H. Dimensionality of collective pinning in 2*H*-$NbSe_2$ single crystals. *Phys. Rev. B* **56,** 3425–3432 (1997).
29. Schmid, A. & Hauger, W. On the theory of vortex motion in an inhomogeneous superconducting film. *J. Low Temp. Phys.* **11,** 667–685 (1973).
30. Bauer, P. *et al.* Depth sensitive visualisation of irradiation-induced columnar defects in 2H-$NbSE_2$. *Euro. Phys. Lett.* **23,** 585–591 (1993).

Supplementary information is available on *Nature*'s World-Wide Web site (http://www.nature.com).

Acknowledgements. We thank A. P. Volodin for developing the first version of our STM, R. J. Drost for auxiliary experiments, M. Konczykowski for carrying out the heavy ion irradiation at GANIL (Caen, France), and M. V. Marchevsky, P. Le Doussal and T. Giamarchi for discussions. This project was partially supported by FOM and the Dutch-Russian Science Collaboration financed by NWO.

Correspondence and requests for materials should be addressed to P.H.K. (e-mail: kes@phys.leidenuniv.nl).

Full sintering of powdered-metal bodies in a microwave field

Rustum Roy, Dinesh Agrawal, Jiping Cheng & Shalva Gedevanishvili

Materials Research Laboratory, The Pennsylvania State University, University Park, Pennsylvania 16802, USA

The use of microwaves to process absorbing materials was studied intensively in the 1970s and 1980s, and has now been applied to a wide variety of materials[1–4]. Initially, success in microwave heating and sintering was confined mainly to oxide and some non-oxide ceramics[5–11]; but recently the technique has been extended to carbide semimetals[12–14] used in cutting tools. Here we describe the microwave sintering of powdered metals to full density. We are able to sinter a wide range of standard powdered metals from commercial sources using a 2.45-GHz microwave field, yielding dense products with better mechanical properties than those obtained by conventional heating. These findings are surprising in view of the reflectivity of bulk metals at microwave frequencies. The ability to sinter metals with microwaves should assist in the preparation of high-performance metal parts needed in many industries, for example, in the automotive industry.

Reviews of microwave processing[1–5] describe its use for materials ranging from wood, bacon and potato chips to rubber, ceramics and semiconductors, but make no mention of metal sintering. Walkiewicz *et al.*[15] exposed a range of materials, including six metals (presumably partly oxidized in air) to a 2.4-GHz field, and reported modest heating (but not sintering), ranging from 120 °C for Mg to 768 °C for Fe. Sintering of tungsten carbide–cobalt composites has also been reported[16]. Nishitani reported[17] that by adding a few per cent of electrically conducting powders such as aluminium, the heating rates of refractory ceramics was considerably enhanced; but no mention was made of the microwave sintering of pure metal powders. Whittaker and Mingos[18] used the highly exothermic (and rapid) reactions of metal powders with sulphur for the microwave-induced synthesis of metal sulphides. German[19] discusses microwave heating of oxide and non-oxide ceramics, but does not mention sintering of metals.

We have used commercial powdered metal components of various alloy compositions—including iron and steel, copper, aluminium, nickel, molybdenum, cobalt, tungsten, tungsten carbide and tin, and their alloys[20]—to obtain essentially fully dense bodies with substantially improved mechanical properties compared to similar bodies sintered by conventional thermal means. Some of these samples were obtained from Keystone Powdered Metal Company (St. Mary, Pennsylvania, USA) and some were made in our laboratory. They were all standard 'green' parts—metal powders cold-pressed with a few per cent of organic binder. The typical size range was 2–5 cm in the largest dimension, with a wide variety of rectangular and cylindrical cross-sections, including typical toothed gears in the 1–4-cm range.

Over the past decade we have developed several specialized